A Compact High-Power Noninverting Bidirectional Buck–Boost Chopper for Onboard Battery Energy Storage Systems

Hamzeh J. Ahmad, *Student Member, IEEE*, and Makoto Hagiwara, *Senior Member, IEEE*

***Abstract*—This article proposes a noninverting bidirectional buck–boost chopper accompanied by an auxiliary converter for battery storage that is installed in a light rail vehicle. The proposed chopper is composed of two half-bridge cells called the main converter, an auxiliary converter consisting of many full-bridge converters connected in cascade, and a small-sized inductor. It is controlled such that the capacitors of the auxiliary converter store and release most of the chopper energy instead of relying solely on a bulky and heavy inductor. As a result, it is lighter and smaller than the four-switch noninverting buck–boost chopper. The operation, as well as the control of the proposed chopper, are experimentally tested using a down-scaled prototype. Furthermore, a comparison with the four-switch noninverting buck–boost chopper with respect to mass, volume, and efficiency is made to verify the efficacy of the proposed chopper.**

***Index Terms*—Choppers, onboard energy storage, railway electrification.**

I. Introduction

RECENTLY, considerable attention has been paid to onboard energy storage systems as a result of an increased interest in the applications that utilize them, including electric vehicles, electrified railway vehicles, electric ships, electric boats, and electric aircrafts [1]–[7]. The building blocks of these energy storage systems can be battery cells, ultracapacitors, fuel cells, flywheels, or a combination of them.

Urban rail transit, such as light rail vehicles, is commonly powered by overhead catenary lines with different dc electrification systems that have voltage levels ranging from 600 V to 3 kV, and there are proposals to extend this range up to 9 kV [8], [9]. Powering railway vehicles by overhead lines has negative consequences such as the installation of overhead lines in urban areas, reliance on the grid for the absorption of peak power demands, and dissipation of the regenerative braking energy [10], [11]. To solve these problems, onboard energy storage systems are utilized. In particular, onboard battery energy storage systems (BESSs) can be used for storing regenerative braking energy and supplying it when required, limiting the catenary voltage drop during acceleration, and allowing driving autonomy during emergencies or during the absence of electrification [2], [12].

Manuscript received December 4, 2020; revised March 22, 2021 and June 8, 2021; accepted August 5, 2021. Date of publication August 19, 2021; date of current version October 15, 2021. Recommended for publication by Associate Editor O. Trescases. (*Corresponding author: Hamzeh J. Ahmad.*)

The authors are with the Department of Electrical and Electronic Engineering, Tokyo Institute of Technology, Tokyo 152-8552, Japan (e-mail: ahmad.h.ab@m.titech.ac.jp; hagiwara@ee.e.titech.ac.jp).

Color versions of one or more figures in this article are available at https://doi.org/10.1109/TPEL.2021.3106240.

Digital Object Identifier 10.1109/TPEL.2021.3106240

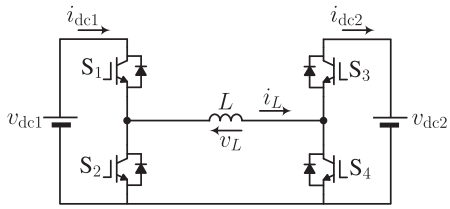

Fig. 1. Four-switch noninverting bidirectional buck–boost chopper (NIBB).

When BESSs are installed on the board of dc electric railways, the mass and volume of the bidirectional chopper become more important because the mass of the onboard chopper influences the driving range, and the volume imposes restrictions on the vehicle design [13]. High-power choppers usually have bulky and heavy magnetics associated with them, where the volume and mass of the chopper are essentially determined by the volume and mass of the energy storage elements required for voltage conversion. In high-power choppers, the dominant burden is the volume and mass of the inductor [14]. To downsize the magnetics, it is required to operate the switching devices at high switching frequencies. However, the switching losses of silicon insulated-gate bipolar transistor (Si-IGBTs) restrict the switching frequency of the high-power choppers to about 1 kHz [15]. Specifically, a typical switching frequency for 3.3 kV Si-IGBTs is set to 600 Hz, according to [16]. Furthermore, it is set to less than 2 kHz even when 3.3 kV silicon carbide MOSFETs are used, according to [17].

If the BESS operates at voltages that go above and below the catenary voltage, (it becomes mandatory to utilize a chopper that can step up and step down the voltage), such as the four-switch noninverting bidirectional buck–boost chopper (NIBB) [18]–[21]. Fig. 1 shows the circuit diagram of the NIBB, which is utilized in applications such as the battery-powered light rail vehicle called SWIMO, where its catenary and BESS voltage levels are 600 and 576 V, respectively [21]. S_1, S_2, S_3, and S_4 are the switching devices of the NIBB, v_{dc1} represents a dc catenary voltage, i_{dc1} denotes the dc current sourced from v_{dc1}, v_{dc2} denotes the voltage that corresponds to a BESS voltage, i_{dc2}

denotes the current that flows to v_{dc2}, L denotes the inductor, v_L denotes the inductor voltage, and i_L denotes the current flowing through the inductor. In the NIBB, a heavy and bulky inductor is used as an energy storage element for voltage conversion.

An interleaved bidirectional chopper that is accompanied by auxiliary converters has been previously proposed by the authors of this article in [22] for reducing the mass and volume of the inductor, where an auxiliary converter comprising many full-bridge cells connected in cascade is applied to the conventional bidirectional chopper. It is characterized by the use of capacitors employed in full-bridge cells to store and release most of the chopper energy instead of relying solely on a bulky and heavy inductor. Because the energy density of capacitors is generally greater than that of inductors, the chopper can be downsized.

The chopper presented in [22] can only operate when the relation $v_{\mathrm{dc1}} > v_{\mathrm{dc2}}$ is satisfied. If this relation is not satisfied, the chopper for the onboard BESS is required to achieve multimode operation including buck mode $(v_{\mathrm{dc1}} > v_{\mathrm{dc2}})$, boost mode $(v_{\mathrm{dc1}} < v_{\mathrm{dc2}})$, and buck–boost mode $(v_{\mathrm{dc1}} \geq v_{\mathrm{dc2}}$ or $v_{\mathrm{dc1}} < v_{\mathrm{dc2}})$. In addition, the control method presented in [22] does not work for the proposed chopper when it operates in boost and buck–boost modes. Therefore, it has to be modified as described later in this article. To the best knowledge of the authors of this article, no study has focused on a noninverting bidirectional buck–boost chopper with an auxiliary converter capable of multimode operation, including experimental verification.

This article aims to demonstrate the validity and effectiveness of the noninverting bidirectional buck–boost chopper with an auxiliary converter, which features multimode operation and a downsized chopper. A down-scaled prototype is used to verify the operation as well as the effectiveness of the control system of the chopper, where experimental waveforms with different modes of operation are shown. To further confirm the validity of the proposed chopper, a comparison with other noninverting bidirectional buck–boost choppers with respect to mass, volume, and efficiency is made.

In this article, the proposed chopper topology is presented in Section II. The working principles of the proposed chopper and its control system are discussed in Sections III and IV, respectively. In Section V, the proposed chopper is compared with other noninverting buck–boost choppers. The experimental results are presented in Section VI. Finally, Section VII concludes this article.

II. Proposed Chopper Topology

The circuit diagram of a noninverting bidirectional buck-boost chopper with an auxiliary converter (NIBAC) is shown in Fig. 2(a). The NIBAC consists of the NIBB, called the main converter, and an auxiliary converter that comprises many full-bridge cells connected in cascade. Fig. 2(b) shows the circuit diagram of a full-bridge cell. v_{C1}, v_{C2}, and v_{CN} denote the capacitor voltages, N denotes the number of full-bridge cells, and v_{A} denotes the voltage produced by the auxiliary converter. v_{M1} and v_{M2} denote the voltages produced by the half-bridge cells that are connected to v_{dc1} and v_{dc2}, respectively. In Fig. 2(b),

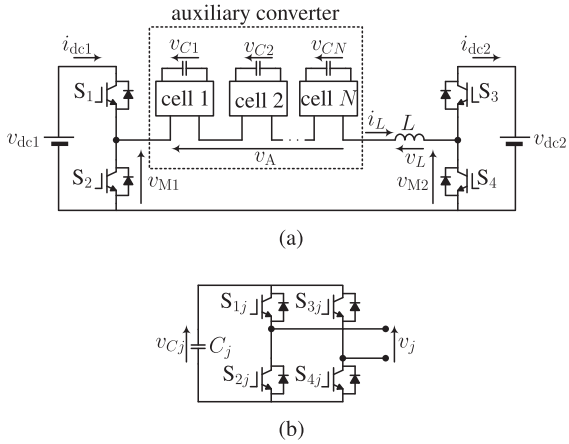

Fig. 2. Noninverting bidirectional buck–boost chopper with an auxiliary converter (NIBAC). (a) Circuit diagram. (b) Full-bridge cell.

C_j (j: 1–N) denotes the dc capacitor, and v_{Cj} and v_j are the dc-capacitor voltage and the output voltage, respectively. S_{1j}, S_{2j}, S_{3j}, and S_{4j} denote the switching devices.

It is noteworthy that the combination of high- and low-voltage switching devices applies to the NIBAC. For example, if the nominal catenary voltage is 1.5 kV, high-voltage switching devices are used for the main converter, whereas low-voltage switching devices can be used for the auxiliary converter. The same combination does not apply to modular multilevel converters (MMCs) for high-voltage applications where the dc-link is more than a hundred kilovolts.

The NIBAC can achieve high reliability by placing redundant cell(s) operating in the standby mode in the auxiliary converter. For example, it is possible to enhance reliability by forming each auxiliary converter with three cells operating in the normal mode and one cell operating in the standby mode. In this case, the output terminals of the redundant cell are short-circuited by means of a mechanical switch; hence, no substantial power loss is produced by the redundant cell, where it is only used when one of the cells operating in the normal mode fails. A similar technique is used in the MMCs [28]. This technique applies to the NIBAC because the operation of each cell in the auxiliary converter is the same.

III. Working Principles

A. Operating Modes of the NIBB

The following describes the operating modes of the conventional NIBB shown in Fig. 1, because the operating modes of the NIBAC as a chopper are identical to those of the NIBB. In an actual BESS, v_{dc1} corresponds to the dc-grid voltage, v_{dc2} corresponds to the battery voltage, and the former can be higher or lower than the latter depending on the operating condition. Hence, it is necessary to employ a chopper that can both increase and decrease the voltage. The switching devices S_1 and S_4 of the NIBB operating in buck–boost mode are typically switched ON or OFF simultaneously. Furthermore, the switching loss in all the switching devices occurs in the buck–boost mode.

To lower the switching losses of the switching devices, the NIBB can be operated in buck mode when $v_{\rm dc1}$ is sufficiently higher than $v_{\rm dc2}$, where this mode is realized by keeping S_3 ON and keeping S_4 OFF while S_1 and S_2 are switched ON and OFF complementarily. Similarly, when $v_{\rm dc1}$ is sufficiently lower than $v_{\rm dc2}$, the NIBB can be operated in boost mode by keeping S_1 ON and keeping S_2 OFF while S_3 and S_4 are switched ON and OFF complementarily. The NIBAC should have the ability to operate in the aforementioned different modes to maintain the advantage of reduced switching losses obtained from the multimode operation.

B. Working Principle of the Main Converter

In the following analysis, the switching devices are assumed to be ideal switches with no loss and zero transition period. When the auxiliary converter is excluded from the NIBAC, the voltage across the inductor during buck mode, $(v_L)_{\rm bk}$, is given by

$$(v_L)_{\rm bk} = \begin{cases} v_{\rm dc1} - v_{\rm dc2} & (S_1: \text{ ON},\ S_2: \text{ OFF}) \\ -v_{\rm dc2} & (S_1: \text{ OFF},\ S_2: \text{ ON}). \end{cases} \quad (1)$$

The voltage across the inductor during the buck–boost mode, $(v_{\rm L})_{\rm bb}$, is given by

$$(v_L)_{\rm bb} = \begin{cases} v_{\rm dc1} & (S_1, S_4: \text{ ON},\ S_2, S_3: \text{ OFF}) \\ -v_{\rm dc2} & (S_1, S_4: \text{ OFF},\ S_2, S_3: \text{ ON}). \end{cases} \quad (2)$$

The voltage across the inductor during the boost mode, $(v_{\rm L})_{\rm bt}$, is given by

$$(v_L)_{\rm bt} = \begin{cases} v_{\rm dc1} - v_{\rm dc2} & (S_3: \text{ ON},\ S_4: \text{ OFF}) \\ v_{\rm dc1} & (S_3: \text{ OFF},\ S_4: \text{ ON}). \end{cases} \quad (3)$$

Regardless of the mode of operation, the voltage across the inductor is a rectangular waveform that has a frequency of $f_{\rm SM}$, owing to the fact that S_1 in a buck or buck–boost mode, and S_3 in boost mode, switch at a frequency of $f_{\rm SM}$. In high-power applications, $f_{\rm SM}$ is limited to low values (e.g., less than 1 kHz) to reduce the switching loss. As a result, the ripple current that occurs in i_L becomes substantial.

C. Working Principle of the Auxiliary Converter

The inductor voltage v_L produces a ripple current that flows through L. To ideally achieve total elimination of the ripple current, the auxiliary converter should be controlled such that it produces a voltage $v_{\rm A}$ that is equal to v_L when the auxiliary converter is excluded from the NIBAC as given by (1), (2), or (3) depending on the mode of operation. Consequently, v_L becomes ideally zero, and i_L becomes ideally pure dc.

The conduction states of the NIBAC operating in buck mode are shown in Fig. 3. In this mode, S_3 is kept ON, and S_4 is kept OFF. Fig. 3(a) and (b) shows the conduction states when i_L is positive. When S_1 is ON and S_2 is OFF, $v_{\rm A}$ is regulated to $v_{\rm dc1} - v_{\rm dc2}$, which makes v_L zero. When S_1 is OFF and S_2 is ON, $v_{\rm A}$ is regulated to $-v_{\rm dc2}$, which makes v_L zero. Fig. 4 shows the ideal waveforms of the NIBAC operating in buck mode.

The conduction states of the NIBAC operating in buck–boost mode are shown in Fig. 5. In this mode, S_1 and S_4 are switched ON and OFF simultaneously, and S_2 and S_3 are switched simultaneously in a switching state opposite to that of S_1 and S_4. It should be noted that the switching frequencies of S_1 and S_2 can be different from those of S_3 and S_4. However, the advantage of using different switching frequencies is little because $v_{\rm dc1}$ is close to $v_{\rm dc2}$ in the buck–boost mode. Fig. 5(a) and (b) shows the conduction states when i_L is positive. When S_1 and S_4 are ON, and S_2 and S_3 are OFF, $v_{\rm A}$ is regulated to $v_{\rm dc1}$, which makes v_L zero. When S_1 and S_4 are OFF, and S_2 and S_3 are ON, $v_{\rm A}$ is regulated to $-v_{\rm dc2}$, which makes v_L zero. Fig. 6 shows the ideal waveforms of the NIBAC operating in buck–boost mode.

The conduction states of the NIBAC operating in boost mode are shown in Fig. 7. In this mode, S_1 is kept ON, and S_2 is kept OFF. Fig. 7(a) and (b) shows the conduction states when i_L is positive. When S_4 is ON and S_3 is OFF, $v_{\rm A}$ is regulated to $v_{\rm dc1}$, which makes v_L zero. When S_4 is OFF and S_3 is ON, $v_{\rm A}$ is regulated to $v_{\rm dc1} - v_{\rm dc2}$, which makes v_L zero. Fig. 8 shows the ideal waveforms of the NIBAC operating in boost mode.

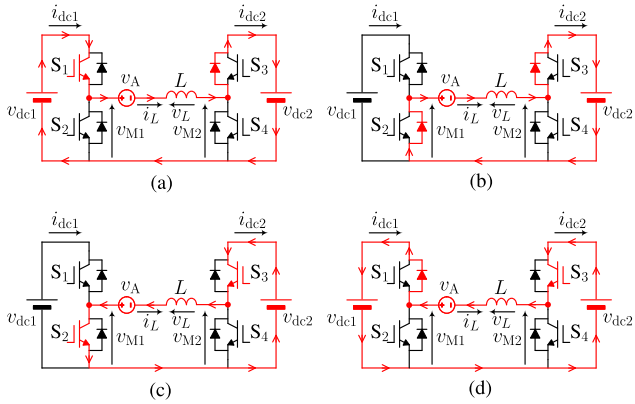

Fig. 3. Four conduction states of the NIBAC operating in buck mode where S_3 is kept ON and S_4 is kept OFFwhen (a) S_1 is ON, and $i_L > 0$, (b) S_2 is ON, and $i_L > 0$, (c) S_2 is ON, and $i_L < 0$, (d) S_1 is ON, and $i_L < 0$.

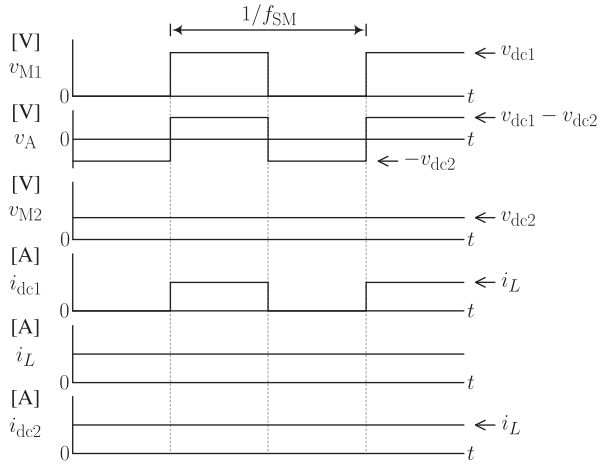

Fig. 4. Ideal waveforms of the NIBAC operating in buck mode.

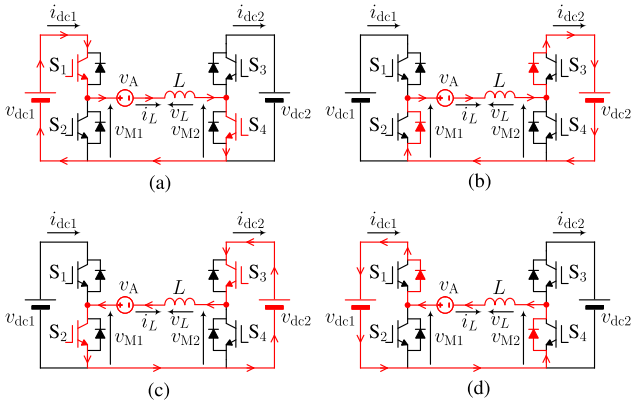

Fig. 5. Four conduction states of the NIBAC operating in buck–boost mode when (a) S_1 and S_4 are ON, and $i_L > 0$, (b) S_2 and S_3 are ON, and $i_L > 0$, (c) S_2 and S_3 are ON, and $i_L < 0$, (d) S_1 and S_4 are ON, and $i_L < 0$.

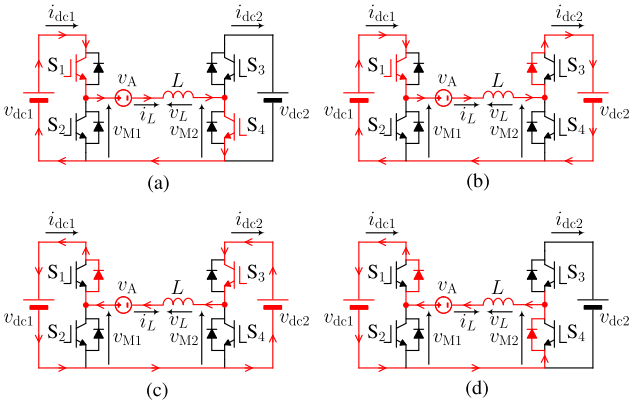

Fig. 7. Four conduction states of the NIBAC operating in boost mode where S_1 is kept ON and S_2 is kept OFF when (a) S_4 is ON, and $i_L > 0$, (b) S_3 is ON, and $i_L > 0$, (c) S_3 is ON, and $i_L < 0$, (d) S_4 is ON, and $i_L < 0$.

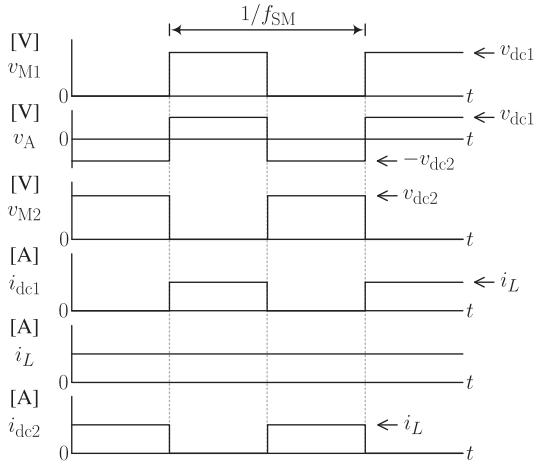

Fig. 6. Ideal waveforms of the NIBAC operating in buck–boost mode.

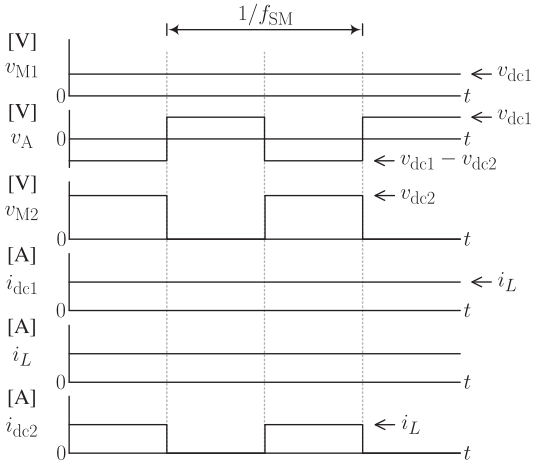

Fig. 8. Ideal waveforms of the NIBAC operating in boost mode.

The ac voltage component that needs to be produced by the auxiliary converter, $v_{\rm A}^*$, in each mode can be given as

$$v_{\rm A}^* = \begin{cases} (v_L)_{\rm bk} & \text{buck mode} \\ (v_L)_{\rm bb} & \text{buck}-\text{boost mode} \\ (v_L)_{\rm bt} & \text{boost mode.} \end{cases} \tag{4}$$

Consequently, pure dc current flows through L. However, in an actual realization of the chopper, the auxiliary converter produces a voltage that contains two ac voltage components: one is added to the positive voltage level, and the other is added to the negative voltage level. For example, $v_{\rm A}$ in Fig. 4 has a positive voltage level with a dc component of $v_{\rm dc1} - v_{\rm dc2}$. In the actual operation of the auxiliary converter, this voltage contains an additional ac voltage component that has a frequency of $2Nf_{\rm SA}$ and a voltage step of v_{Cj} because a phase-shifted pulsewidth modulation (PSPWM) is utilized [23]. This ac voltage component generates a ripple current in i_L. However, this ripple current can be attenuated with a much smaller inductor.

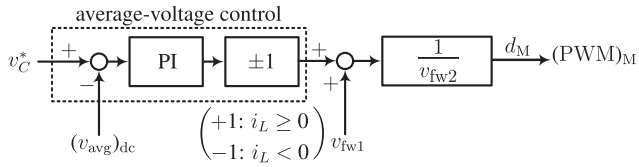

Fig. 9. Main converter control subsystem.

IV. Chopper Control

The control system of the NIBAC consists of two subsystems, one for the main converter and the other for the auxiliary converter. The main converter control regulates the average value of all capacitor voltages, whereas, the auxiliary converter control regulates i_L, balances the capacitor voltages, and produces $(v_{\rm A})_{\rm ac}$.

A. Main Converter Control

The block diagram that represents the control subsystem of the main converter is shown in Fig. 9. The average-voltage control loop regulates the average value of all capacitor voltages,

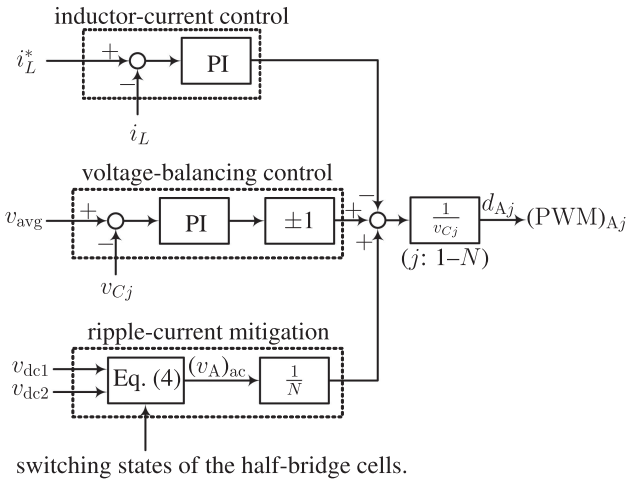

Fig. 10. Auxiliary converter control subsystem.

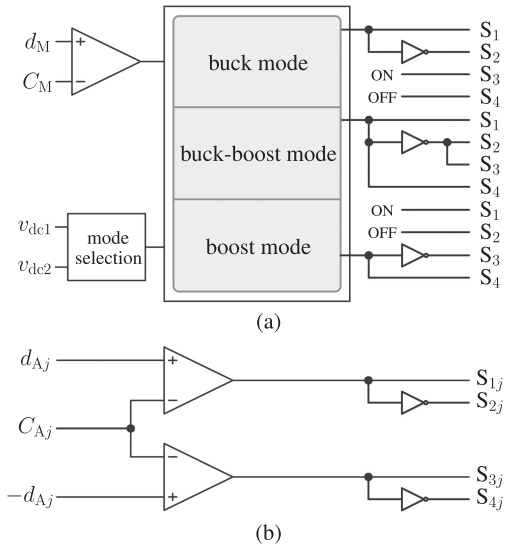

Fig. 11. Block diagram for the generation of the switching states of the switching devices of (a) full-bridge cells and (b) half-bridge cells.

$(v_{\rm avg})_{\rm dc}$, to its reference v_C^*, where $v_{\rm avg}$ is given by

$$v_{\rm avg} = \frac{1}{N}\sum_{j=1}^{N} v_{Cj} \tag{5}$$

where $(v_{\rm avg})_{\rm dc}$ is computed by utilizing a moving-average filter that has a frequency of $f_{\rm SM}$. The polarity of the output of the PI controller of the average-voltage control should be changed according to that of i_L. $v_{\rm fw1}$ is used as a feedforward control signal, where the sum of $v_{\rm fw1}$ and the output of the PI controller of the average-voltage control after adjusting its polarity is divided by $v_{\rm fw2}$, producing $d_{\rm M}$, which is fed to a pulsewidth modulator $({\rm PWM})_{\rm M}$. Here, $v_{\rm fw1}$ and $v_{\rm fw2}$ are feedforward signals that are given by (6) and (7), respectively, where the feedforward signals are changed depending on the mode of operation

$$v_{\rm fw1} = \begin{cases} v_{\rm dc2} & {\rm buck\,mode} \\ v_{\rm dc2} & {\rm buck{-}boost\,mode} \\ v_{\rm dc2} - v_{\rm dc1} & {\rm boost\,mode} \end{cases} \tag{6}$$

$$v_{\rm fw2} = \begin{cases} v_{\rm dc1} & {\rm buck\,mode} \\ v_{\rm dc1} + v_{\rm dc2} & {\rm buck{-}boost\,mode} \\ v_{\rm dc2} & {\rm boost\,mode.} \end{cases} \tag{7}$$

The quotient $v_{\rm fw1}/v_{\rm fw2}$ is added to accelerate the convergence of the control loops, where it gives the duty ratio required to ensure power balance between $v_{\rm dc1}$ and $v_{\rm dc2}$. The auxiliary converter does not affect the power balance since it neither consumes nor supplies average active power. Assuming ideal components and constant $v_{\rm dc1}$ and $v_{\rm dc2}$, the average power supplied/consumed by $v_{\rm dc1}$ equals the average power supplied/consumed by $v_{\rm dc2}$, where this power balance can be described by

$$v_{\rm dc1}(i_{\rm dc1})_{\rm avg} = v_{\rm dc2}(i_{\rm dc2})_{\rm avg} \tag{8}$$

where $(i_{\rm dc1})_{\rm avg}$ and $(i_{\rm dc2})_{\rm avg}$ are the average values of $i_{\rm dc1}$ and $i_{\rm dc2}$, respectively. For buck mode, $(i_{\rm dc1})_{\rm avg} = d_{\rm M} i_L$, $(i_{\rm dc2})_{\rm avg} = i_L$, where $d_{\rm M}$ is the duty ratio of S_1. For boost mode, $(i_{\rm dc1})_{\rm avg} = i_L$, $(i_{\rm dc2})_{\rm avg} = (1-d_{\rm M})i_L$, where $d_{\rm M}$ is the duty ratio of S_4. For buck–boost mode, $(i_{\rm dc1})_{\rm avg} = d_{\rm M} i_L$, $(i_{\rm dc2})_{\rm avg} = (1-d_{\rm M})i_L$, where $d_{\rm M}$ is the duty ratio of S_1 and S_3. Substituting $(i_{\rm dc1})_{\rm avg}$ and $(i_{\rm dc2})_{\rm avg}$ in (8), large-signal $d_{\rm M}$ can be found which is defined as $v_{\rm fw1}/v_{\rm fw2}$. In an actual converter operation, an additional component is added to $v_{\rm fw1}/v_{\rm fw2}$ by the control system to account for losses.

The block diagram for the generation of the switching states of the switching devices of the half-bridge cells is shown in Fig. 11(a), where $d_{\rm M}$ is compared with a triangular carrier, and the switching states of the switching devices are determined depending on the mode of operation, which is selected based on the relation between $v_{\rm dc1}$ and $v_{\rm dc2}$ as demonstrated in Section III. The carrier of the main converter, $C_{\rm M}(t)$, as a function of time, t, is a triangular carrier that has a frequency of $f_{\rm SM}$ as described by (9), where the frac function is defined as ${\rm frac}(x) = x - \lfloor x \rfloor$, $\lfloor x \rfloor$ is the floor of x, and $\theta_{\rm M}$ is the initial phase of the carrier in radians

$$C_{\rm M}(t) = 1 - \left| 2{\rm frac}\left(\frac{2\pi f_{\rm SM} t + \theta_{\rm M}}{2\pi}\right) - 1 \right|. \tag{9}$$

B. Auxiliary Converter Control

The block diagram that represents the control subsystem of the auxiliary converter is shown in Fig. 10. The power flow between $v_{\rm dc1}$ and $v_{\rm dc2}$ can be indirectly controlled by controlling i_L, where the inductor-current control loop regulates i_L to its reference i_L^*. The voltage-balancing control loop regulates each capacitor voltage, v_{Cj}, to its $v_{\rm avg}$, where the dc component of $v_{\rm avg}$ is controlled by the main converter control to equal v_C^*. The ripple current can be attenuated by generating a voltage $v_{\rm A}^*$ given by (4), where $v_{\rm dc1}$, $v_{\rm dc2}$, and the switching states of the switching devices of the half-bridge cells are used as feedforward inputs, where each full-bridge cell generates an ac voltage of $(v_{\rm A})_{\rm ac}/N$. Finally, the duty ratios of the full-bridge cells, $d_{{\rm A}j}$, are fed to pulsewidth modulators $({\rm PWM})_{{\rm A}j}$, where a PSPWM is applied. Fig. 11(b) shows the block diagram for

the generation of the switching states of the switching devices of the auxiliary converter.

For the auxiliary converter to be able to generate the ac voltage that is given by (4), the following relation should be satisfied:

$$-Nv_{Cj} \le v_{\rm A} \le Nv_{Cj}. \tag{10}$$

From (4) and (10), v_{Cj} should satisfy the following conditions:

$$\begin{cases} \dfrac{v_{\rm dc1}}{N} \le v_{Cj} \\ \dfrac{v_{\rm dc2}}{N} \le v_{Cj}. \end{cases} \tag{11}$$

The capacitance of each full-bridge cell capacitor should be selected such that the capacitor ripple voltage is maintained within a certain limit. For buck mode, the capacitor ripple voltage, $(v_{Cj})_{\rm ripple}$, can be given as

$$(v_{Cj})_{\rm ripple} = \frac{d_{\rm M}(v_{\rm dc1} - v_{\rm dc2})i_L}{NC_j f_{\rm SM}(v_{Cj})_{\rm dc}}. \tag{12}$$

For boost and buck–boost modes, the capacitor ripple voltage, $(v_{Cj})_{\rm ripple}$, can be given as

$$(v_{Cj})_{\rm ripple} = \frac{d_{\rm M} v_{\rm dc1} i_L}{NC_j f_{\rm SM}(v_{Cj})_{\rm dc}} \tag{13}$$

where $(v_{Cj})_{\rm dc}$ is the value of the dc component of v_{Cj}.

The carriers of the full-bridge cells are triangular carriers that have a frequency of $f_{\rm SA}$ and are phase-shifted by (π/N) relative to each other, where the following equations describe the carriers and the phase-shift between the carriers

$$C_{{\rm A}j}(t) = 1 - \left|4{\rm frac}\left(\frac{2\pi f_{\rm SA} t + \theta_{{\rm A}j}}{2\pi}\right) - 2\right| \tag{14}$$

$$\theta_{{\rm A}j} = \theta_{\rm M} + \frac{\pi(j-1)}{N} \tag{15}$$

where $C_{{\rm A}j}(t)$ is the carrier associated with the jth full-bridge cell and $\theta_{{\rm A}j}$ is the initial phase of the jth carrier in radians.

To illustrate the working principle of the PSPWM that is applied to the NIBAC, an auxiliary converter with two full-bridge cells is used as an example as shown in Fig. 12(a). Fig. 12(b)–(k) shows the different conduction states of the two full-bridge cells when the NIBAC operates in buck–boost mode. Fig. 13 shows the ideal waveforms of the circuit shown in Fig. 12(a), where v_{C1} and v_{C2} are assumed constant and the effect of the capacitor-voltage ripple is ignored. The letters b to k indicate the operating conduction state during each period. It can be shown from Fig. 13 that $v_{\rm A}$ has a low-frequency ac voltage component with a frequency of $f_{\rm SM}$, and a high-frequency ac voltage component with a frequency of $2Nf_{\rm SA}$. When $v_{\rm M1} = v_{\rm dc1}$, $v_{\rm L}$ switches between $v_{\rm dc1} - v_{C1} - v_{C2}$ and $v_{\rm dc1} - v_{C1}$ with a frequency of $2Nf_{\rm SA}$. Assuming that $v_{C1} = v_{C2}$, the voltage step of the inductor voltage is v_{Cj}. Similarly, when $v_{\rm M1} = 0$, $v_{\rm L}$ switches between $-v_{\rm dc2} - v_{C1} - v_{C2}$ and $-v_{\rm dc2} - v_{C1}$ with a frequency of $2Nf_{\rm SA}$ and a voltage step of v_{Cj}. Consequently, only the high-frequency component appears across L and generates ripple current.

The minimum equivalent switching frequency of the auxiliary converter should be equal to or higher than the switching frequency of the main converter. However, to cancel out the ac component of $v_{\rm M1} - v_{\rm M2}$ that has a frequency of $f_{\rm SM}$, the equivalent switching frequency of the auxiliary converter should be high enough. As a practical value, it is advised to be ten times of $f_{\rm SM}$ or more.

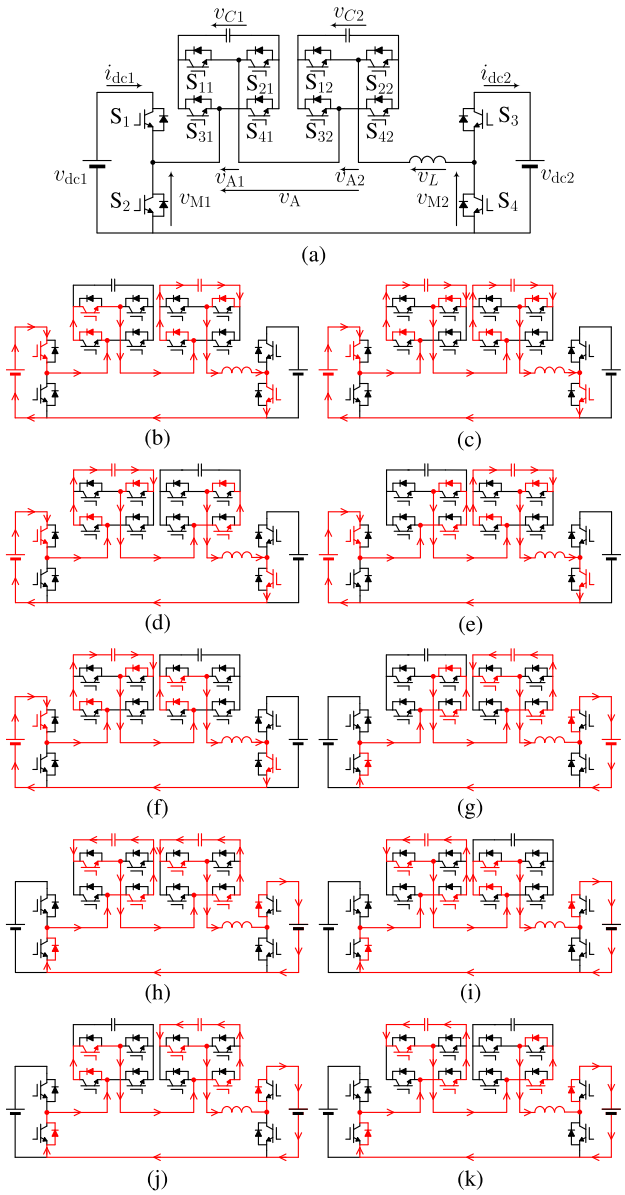

Fig. 12. Illustration of the conduction states of the main and auxiliary converters when the NIBAC operates in buck–boost mode. (a) Circuit configuration. (b) to (k) are the conduction states.

It should be noted that for the NIBAC to commence its operation, all full-bridge cell capacitors need to have an initial voltage of v_C. It is possible to achieve the initial charging without additional circuits. For example, a method based on the sequential charging presented in [22] can be applied to the NIBAC to charge its capacitors from $v_{\rm dc1}$ with S_3 turned OFF and S_4 turned ON. Because the initial charging method of capacitors is not the main focus of this article, the initial charging will not be further described in the following.

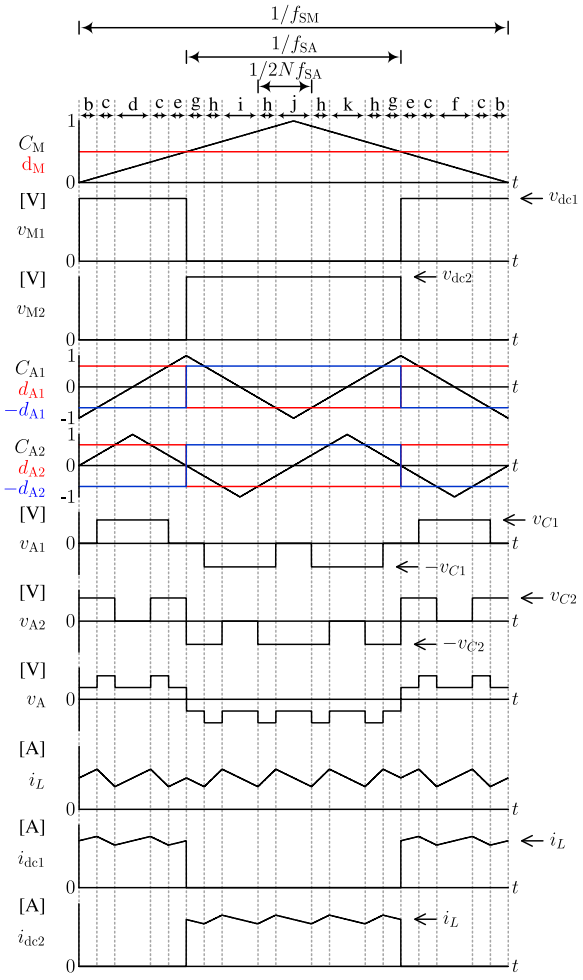

Fig. 13. Ideal waveforms of the NIBAC shown in Fig. 12(a) operating in buck–boost mode.

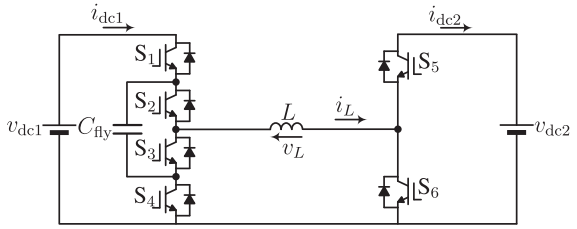

Fig. 14. Three-level noninverting buck–boost chopper (TL-NIBB).

TABLE I
PARAMETERS OF THE CHOPPERS FOR COMPARISON

Power rating	P	75 kW
Voltage source 2	v_{dc2}	1.0 kV
Inductance (NIBB)	L	44.0 mH
Inductance (TL-NIBB)	L	22.5 mH
Inductance (NIBAC)	L	0.75 mH
Full-bridge count	N	3
Voltage of the full-bridge cell capacitor	v_C	0.5 kV
Full-bridge cell capacitor	C_j	2.46 mF
Flying capacitor	C_{fly}	2.44 mF
Carrier frequency (half-bridge)	f_{SM}	900 Hz
Carrier frequency (three-level leg)	f_{TL}	450 Hz
Carrier frequency (full-bridge)	f_{SA}	3.6 kHz

V. COMPARISON

It has been stated earlier in this article that the NIBAC relies on the capacitors that are attached to the full-bridge cells to store and release the energy of the chopper during voltage conversion. It has been argued that because the energy density of the capacitors is generally greater than that of the inductors, it is possible to downsize the chopper. To demonstrate the strength of this argument, a comparison between the NIBAC and two other noninverting buck–boost choppers with respect to mass and volume is carried out. The cost comparison is beyond the scope of this article and left for future work. These choppers are the NIBB that is shown in Fig. 1, and the three-level noninverting buck–boost chopper (TL-NIBB) that is shown in Fig. 14 [24].

TL-NIBB is formed by replacing the two-level leg of the NIBB (i.e., S_1 and S_2 in Fig. 1) by a three-level flying capacitor leg (S_1, S_2, S_3, S_4, and a flying capacitor, C_{fly}, in Fig. 14). The switching frequency of the switching devices of the three-level leg, f_{TL}, should be half the switching frequency of the switching devices of the two-level leg, f_{SM}. Besides, the voltage of the flying capacitor is controlled to be $v_{\mathrm{dc1}}/2$.

For a fair comparison, the choppers are designed as follows.

1) For all choppers, $P = 75$ kW, $v_{\mathrm{dc2}} = 1.0$ kV, and $f_{\mathrm{SM}} = 900$ Hz. For the three-level leg of the TL-NIBB, $f_{\mathrm{TL}} = 450$ Hz which makes the equivalent switching frequency f_{SM}, and $C_{\mathrm{fly}} = 2.44$ mF. For the NIBAC, $C_j = 2.46$ mF.
2) v_{dc1} has a range from 0.5 to 1.5 kV.
3) All choppers operate in boost mode when $v_{\mathrm{dc1}} < 0.9$ kV, in buck-boost mode when 0.9 kV$\leq v_{\mathrm{dc1}} \leq 1.1$ kV, and in buck mode when $v_{\mathrm{dc1}} > 1.1$ kV.
4) The maximum peak-to-peak ripple current is approximately 13 A for all choppers. This value occurs at $v_{\mathrm{dc1}} = 1.23$ kV with $L = 0.75$ mH for the NIBAC, $v_{\mathrm{dc1}} = 1.10$ kV with $L = 22.5$ mH for the TL-NIBB, and $v_{\mathrm{dc1}} = 1.10$ kV with $L = 44$ mH for the NIBB.

Table I summarizes the parameters of all choppers that are used for the comparison. After their parameters were set, their components were selected. Air-core inductors were selected because they are widely employed in choppers for railways [25]. The three inductors obey the Brooks coil geometry, which was adopted because it gives the highest possible inductance for a given length of wire [26]. The parameters of the designed inductors are summarized in Table II, where the definitions of the symbols of the parameters are provided in the Appendix.

For the NIBAC, a 700 V, 0.82 mF dc film capacitor (E50.N15-824NT0) was selected for the full-bridge cells, where a parallel connection of three capacitors was utilized, which gives an equivalent capacitance of 2.46 mF. For the TL-NIBB, a parallel connection of four 900 V, 0.61 mF dc film capacitors (E50.N15-614NT0) was selected, which makes the capacitance of the flying capacitor 2.44 mF. The specifications of the selected capacitors can be found in [31].

The IGBT power module, MBM250H33E3 (Si-IGBT, 2-in-1, 3.3 kV), was selected for all choppers, where two modules were

TABLE II
PARAMETERS OF THE AIR-CORE INDUCTORS

Parameter	NIBB	TL-NIBB	NIBAC
L	44.0 mH	22.5 mH	0.75 mH
a	28.06 cm	23.94 cm	13.32 cm
b	19.28 cm	17.01 cm	7.94 cm
c	20.41 cm	18.14 cm	9.07 cm
d	10.4 mm	10.4 mm	10.4 mm
d_i	11.3 mm	11.3 mm	11.3 mm
n_l	18	16	8
n_t	17	15	7
n	306	240	56
m_{ir}	410.69 kg	274.78 kg	35.67 kg
v_{ir}	88.70 dm^3	58.24 dm^3	7.95 dm^3
R_{dc}	109.3 mΩ	73.10 mΩ	9.5 mΩ

used for the NIBB, two modules were used for the main converter of the NIBAC, and one module was used for the two-level leg of the TL-NIBB. The IGBT power module, 2MBI200XAA120-50 (Si-IGBT, 2-in-1, 1.2 KV), was selected for the NIBAC and the TL-NIBB, where six modules were used for the full-bridge cells of the NIBAC and two modules were used to form the three-level leg of the TL-NIBB. The specifications of MBM250H33E3 and 2MBI200XAA120 are given in [29] and [30], respectively.

The worst-case losses of the switching devices which occur at $v_{\mathrm{dc1}} = 0.9$ kV, were estimated based on the loss characteristics obtained from their datasheets, where the loss characteristics for each power device were scaled based on the voltage, current, and junction temperature that was estimated by establishing thermal resistance networks that describe the heat distribution in the switching devices. The method for estimating the power losses is conventional and well-known in the literature. Fig. 15 shows the thermal resistance networks that were used for the calculation of the junction temperatures.

The cooling systems of the NIBB, main converter of the NIBAC, and the two-level leg of the TL-NIBB were designed such that each MBM250H33E3 module is mounted on a single heatsink as depicted in Fig. 15(a), where P_{Q1} and P_{D1} are the power losses of the upper IGBT and the upper diode of the module, respectively. P_{Q2} and P_{D2} are the power losses of the lower IGBT and the lower diode of the module, respectively. T_{jQ1}, T_{jD1}, T_{jQ2}, and T_{jD2} are the junction temperatures of the upper IGBT, upper diode, lower IGBT, and lower diode, respectively. $(R_{\mathrm{jc}})_{\mathrm{Q}}$ and $(R_{\mathrm{jc}})_{\mathrm{D}}$ are the junction-to-case thermal resistances of the IGBT and diode, respectively. T_{c} is the case temperature. R_{cs} is the case-to-sink thermal resistance, where this parameter is given for the whole module in [29]. T_{s} is the heatsink temperature. R_{sa} is the sink-to-ambient thermal resistance. T_{a} is the ambient temperature.

The cooling systems of the full-bridge cells of the NIBAC and the three-level leg of the TL-NIBB were designed such that every two 2MBI200XAA120-50 modules are mounted on a single heatsink as depicted in Fig. 15(b), where P_{Q1}, P_{D1}, P_{Q2}, and P_{D2} are the power losses of the first module, and P_{Q3}, P_{D3}, P_{Q4}, and P_{D4} are the power losses of the second module. T_{jQ1}, T_{jD1}, T_{jQ2}, and T_{jD2} are the junction temperatures of the switching devices of the first module, and T_{jQ3}, T_{jD3}, T_{jQ4}, and T_{jD4} are the junction temperatures of the switching devices of the second module. T_{c1}, T_{c2}, T_{c3}, and T_{c4} are the case temperatures above each IGBT/diode. R_{cs} is given for half module (one IGBT and one diode) in [30].

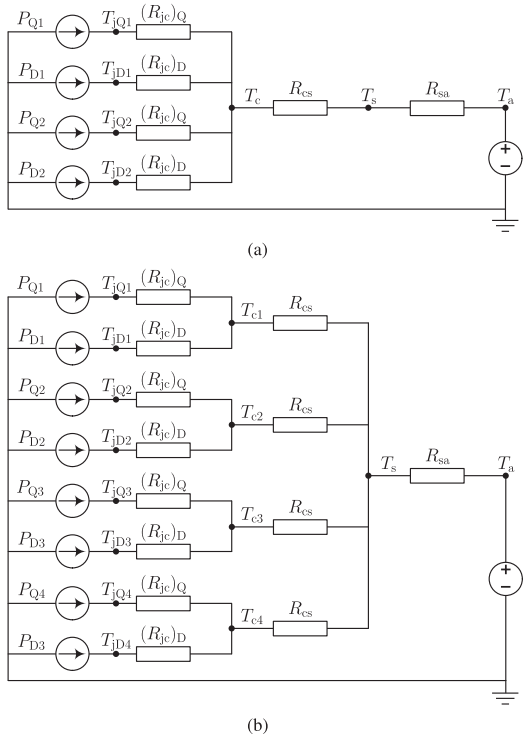

Fig. 15. Thermal resistance networks used for temperature calculations. (a) Single heatsink for one MBM250H33E3 module. (b) Single heatsink for two 2MBI200XAA120-50 modules.

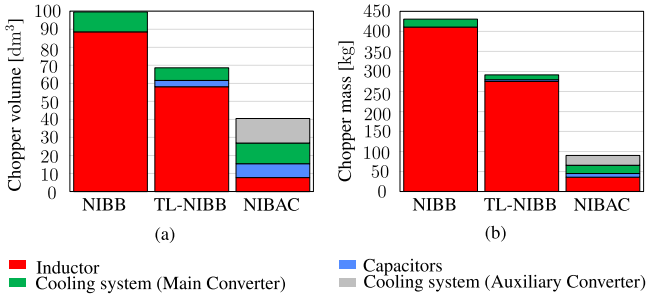

Fig. 16. Comparison of choppers with respect to (a) volume and (b) mass.

For an ambient temperature of 40 °C, the cooling system was designed to keep the maximum junction temperature of the switching devices less than or equal to 125 °C. After that, the volume of the heatsinks was calculated by assuming that the cooling system performance index (CSPI) is 7.0 [27]. To obtain an approximate estimate of the mass of the heatsinks, their density is assumed to be two-third the density of aluminum.

The mass of each chopper was estimated by calculating the sum of the masses of its components, and the volume of each chopper was estimated in a similar way. As can be shown in Fig. 16, a reduction of the chopper volume by 59% and a reduction of the chopper mass by 79% can be achieved when

the NIBB is replaced by the NIBAC. Besides, a reduction of the chopper volume by 41% and a reduction of the chopper mass by 69% can be achieved when the TL-NIBB is replaced by the NIBAC. The volumetric power density of the NIBB, TL-NIBB, and the NIBAC are 0.75, 1.10, and 1.84 $\mathrm{kW/dm^3}$, respectively. The mass power density of the NIBB, TL-NIBB, and the NIBAC are 0.17, 0.26, and 0.83 $\mathrm{kW/kg}$, respectively.

The inductors of all choppers were designed to handle the maximum current which occurs when the rated power is delivered when $v_{\mathrm{dc1}} = 0.9$ kV and $v_{\mathrm{dc2}} = 1.0$ kV. Similarly, the highest power losses in the switching devices of the main and auxiliary converters occur at this point as can be inferred from Fig. 17. Therefore, the heatsinks were designed at this point.

A very fair comparison between the choppers in terms of volume and mass requires them to have all of their characteristics other than the mass and volume to be the same. For example, the efficiency curves of all choppers should be identical and their costs should be the same. However, it is very difficult to satisfy these conditions because the three choppers are different in their components and working principles. However, at the operating point that determines the mass and volume of both choppers (i.e., when $v_{\mathrm{dc1}} = 0.9$ kV, $v_{\mathrm{dc2}} = 1.0$ kV, and rated power is delivered), their efficiencies are close to each other. In other words, even if the losses of the NIBB and TL-NIBB are lower than those of the NIBAC in operating conditions other than the operating condition at which the highest power losses occur, it does not mean that the volume and mass of the other converters can be significantly reduced. Therefore, the comparison performed in this section can be regarded as a fair comparison because both choppers are designed to handle a comparable amount of worst-case losses.

The power losses of the choppers are estimated to compare them in terms of efficiency. The loss of the switching devices and the copper loss of the inductors are considered. Fig. 17 shows the loss breakdown of the choppers for different modes of operation. The efficiency of the NIBAC is predicted to be less than that of the other choppers because the former has a higher count of switching devices. Fig. 18 shows the efficiency curves of the choppers for different modes of operation.

It can be concluded from Figs. 16 and 18 that the small reduction in the efficiency of the chopper is insignificant when the significant downsizing of the chopper is taken into account. In addition, the downsizing of the chopper reduces the energy required to move the vehicle, which can eventually improve the overall energy efficiency of the vehicle.

VI. Experimental Results

A. Experimental Verification

To validate the NIBAC operation along with its control system, a down-scaled experimental prototype was built. Fig. 19 shows the experimental setup, where parts of the setup were used to build the prototype. In other words, one auxiliary converter, one inductor, one current sensor, five voltage sensors, three sets of capacitors, two bidirectional chopper cells, and the control board that combines field-programmable gate array (FPGA),

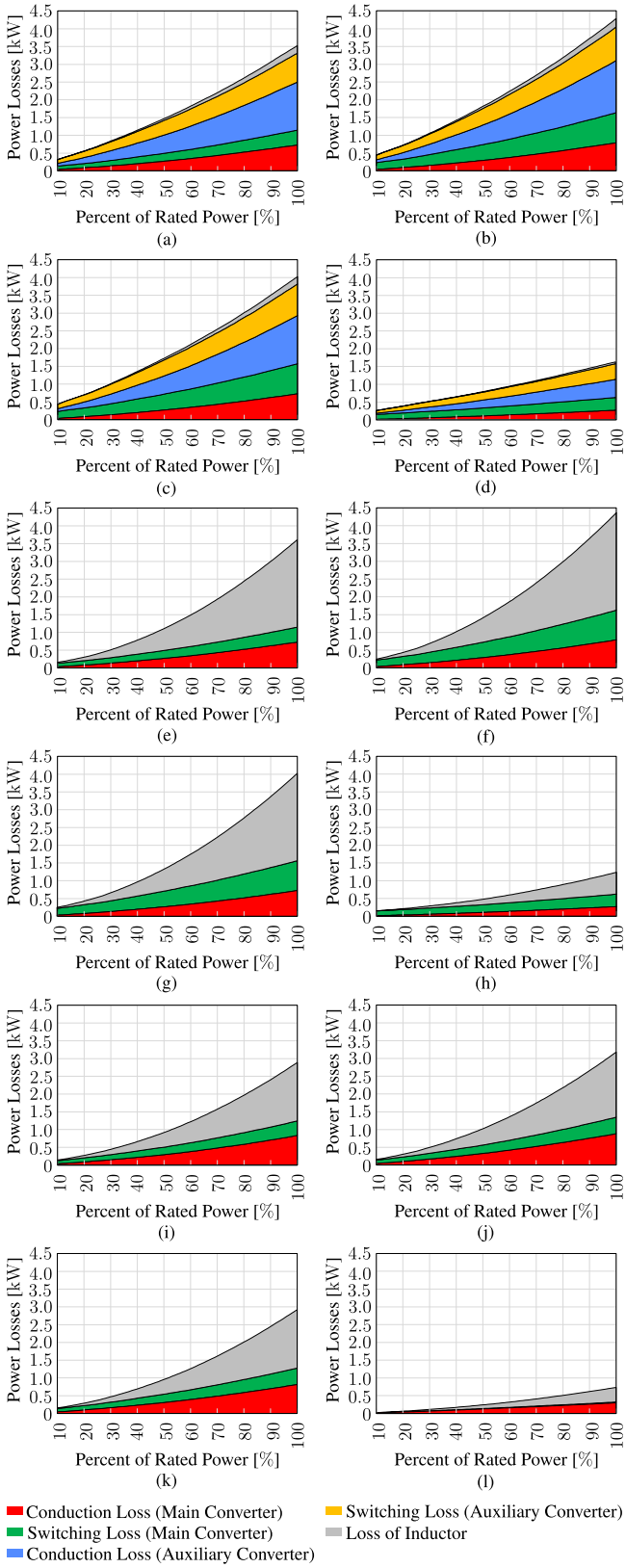

Fig. 17. Loss breakdown of (a) NIBAC when $v_{\mathrm{dc1}} = 0.5$ kV. (b) NIBAC when $v_{\mathrm{dc1}} = 0.9$ kV. (c) NIBAC when $v_{\mathrm{dc1}} = 1.0$ kV. (d) NIBAC when $v_{\mathrm{dc1}} = 1.5$ kV. (e) NIBB when $v_{\mathrm{dc1}} = 0.5$ kV. (f) NIBB when $v_{\mathrm{dc1}} = 0.9$ kV. (g) NIBB when $v_{\mathrm{dc1}} = 1.0$ kV. (h) NIBB when $v_{\mathrm{dc1}} = 1.5$ kV. (i) TL-NIBB when $v_{\mathrm{dc1}} = 0.5$ kV. (j) TL-NIBB when $v_{\mathrm{dc1}} = 0.9$ kV. (k) TL-NIBB when $v_{\mathrm{dc1}} = 1.0$ kV. (l) TL-NIBB when $v_{\mathrm{dc1}} = 1.5$ kV.

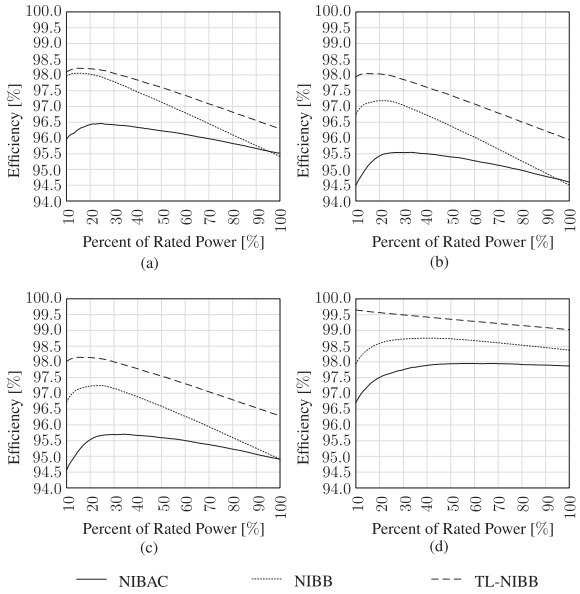

Fig. 18. Efficiency of the choppers for different modes of operation. (a) $v_{\mathrm{dc1}} = 0.5\,\mathrm{kV}$. (b) $v_{\mathrm{dc1}} = 0.9\,\mathrm{kV}$. (c) $v_{\mathrm{dc1}} = 1.0\,\mathrm{kV}$. (d) $v_{\mathrm{dc1}} = 1.5\,\mathrm{kV}$.

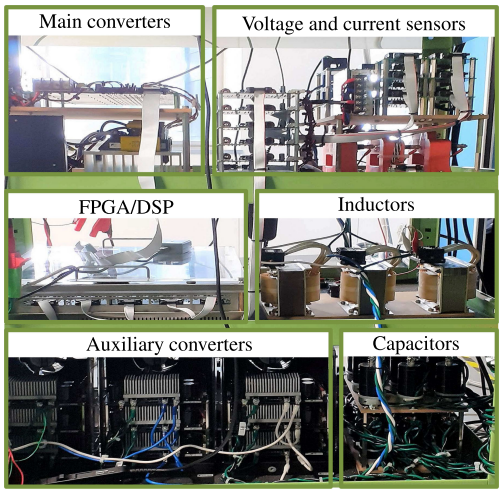

Fig. 19. Photograph of the experimental setup.

digital signal processor (DSP), and analog-to-digital (A/D) converters, were used, whereas the remaining parts were not used. The experimental parameters are summarized in Table III. The following experiments were carried out.

1) Steady-state behavior in buck mode with $v_{\mathrm{dc1}} = 150$ V, $v_{\mathrm{dc2}} = 100$ V, and $i_L^* = 10$ A.
2) Steady-state behavior in buck–boost mode with $v_{\mathrm{dc1}} = 100$ V, $v_{\mathrm{dc2}} = 100$ V, and $i_L^* = 20$ A.
3) Steady-state behavior in boost mode with $v_{\mathrm{dc1}} = 50$ V, $v_{\mathrm{dc2}} = 100$ V, and $i_L^* = 20$ A.
4) Transient-state behavior in buck–boost mode with $v_{\mathrm{dc1}} = 100$ V, $v_{\mathrm{dc2}} = 100$ V, and i_L^* was increased from -20 A to 20 A in 300 ms.
5) Transient-state behavior in buck–boost mode with $i_L = 20$ A, $v_{\mathrm{dc2}} = 100$ V, and a step change in v_{dc1} from 90 to 110 V.

TABLE III
PARAMETERS OF THE PROTOTYPE

Voltage source 1	v_{dc1}	150 V, 100 V, 50 V
Voltage source 2	v_{dc2}	100 V
Inductance at 0 Hz	L (0 Hz)	0.75 mH
Inductance at 21.6 kHz	L (21.6 kHz)	0.32 mH
Full-bridge count	N	3
Voltage of the dc capacitor	v_C	50 V
Full-bridge cell capacitor	C_j	2.5 mF
Carrier frequency (half-bridge)	f_{SM}	900 Hz
Carrier frequency (full-bridge)	f_{SA}	3.6 kHz

In addition, the experimental conditions were as follows.

1) v_{dc1} and v_{dc2} were connected to programmable power sources (NF DP030RS) with a reverse power flow capability.
2) v_{C1}, v_{C2}, and v_{C3} were initially charged to 50 V.
3) The control system of the NIBAC was implemented using a Texas Instruments TMS320C6678 DSP.
4) Altera Cyclone IV FPGA was used to generate the triangular carriers, to compare the duty ratios (i.e., d_{M} and $d_{\mathrm{A}j}$) computed by the DSP and the triangular carriers, to select the mode of operation, and to generate the 16 gate signals.
5) The A/D converters were used to detect v_{dc1}, v_{dc2}, v_{C1}, v_{C2}, v_{C3}, and i_L. All A/D converters were connected to the FPGA and the converted values were handled to the DSP, where the sampling period of the A/D converters and the reference update period of the control system were set to 46.3 μs $(= 1/(2Nf_{\mathrm{SA}}))$.

The experimental waveforms were captured as follows.

1) The experimental waveforms of v_{dc1}, v_{M1}, v_{A}, and v_{M2} were captured by the Tektronix oscilloscope DPO4034B, those of i_{dc1}, i_L, and i_{dc2} were captured by the Tektronix oscilloscope MDO4104 C, and those of v_{C1}, v_{C2}, and v_{C3} were captured by the Tektronix oscilloscope DPO3054.
2) The Tektronix voltage probe THDP0100 was used for the measurement of v_{M1}, TMDP0200 to measure v_{A}, v_{M2}, v_{C1}, v_{C2}, and v_{C3}, and P5205 A to measure v_{dc1}. The Tektronix current probe TCP0150 was used to measure i_{dc1} and i_{dc2}, and TCP0030 A to measure i_L.

B. Steady-State Behavior in Buck Mode

Fig. 20 shows the steady-state behavior of the NIBAC operating in buck mode, where $i_L^* = 10$ A and $v_{\mathrm{dc1}} = 150$ V. As can be seen in Fig. 20, v_{M1} is a rectangular wave that has an ac component and an average dc component. The frequency of the ac component equals f_{SM} (i.e., 900 Hz). It can be observed that the duty ratio of S_1, d_{M}, is slightly larger than two-third $(= v_{\mathrm{dc2}}/v_{\mathrm{dc1}})$ because the average-voltage control adds a voltage component to the feedforward component given by (6). v_{M2} is equal to v_{dc2} because S_3 is kept ON and S_4 is kept OFF during this mode of operation. v_{A}, is a rectangular wave with a principal frequency of 900 Hz. In addition, the PSPWM generates a voltage ripple component that has a frequency of 21.6 kHz $(= 2Nf_{\mathrm{SA}})$ and a voltage step of 50 V $(= v_{Cj})$. The 900-Hz ac components contained within $v_{\mathrm{M1}} - v_{\mathrm{M2}}$ and v_{A} cancel each other out, and only the 21.6 kHz voltage ripple

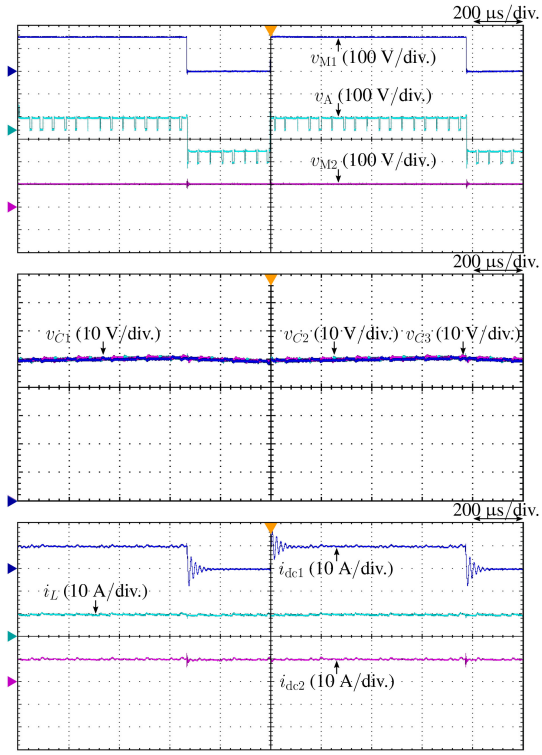

Fig. 20. Experimental waveforms of the NIBAC operating in buck mode.

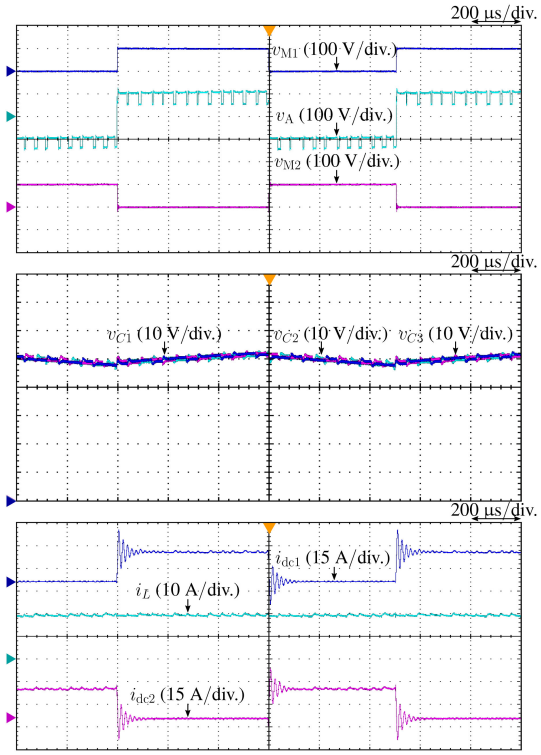

Fig. 21. Experimental waveforms of the NIBAC operating in buck–boost mode.

remains, which results in a significant attenuation of the inductor ripple current.

The dc-capacitor voltages, v_{C1}, v_{C2}, and v_{C3}, contain a 50-V dc component, and a 900-Hz ac component that has a peak-to-peak voltage less than one-tenth of the dc component.

The current sourced from $v_{\rm dc1}$, $i_{\rm dc1}$, is a rectangular wave with a principal frequency of 900 Hz ($=f_{\rm SM}$). Furthermore, the dc current flowing to $v_{\rm dc2}$, $i_{\rm dc2}$, is equal to i_L. The active power flow between $v_{\rm dc1}$ and $v_{\rm dc2}$ is indirectly controlled by controlling i_L. Fig. 20 shows that i_L is regulated at 10 A.

C. Steady-State Behavior in Buck–Boost Mode

The steady-state behavior of the NIBAC during buck-boost operation is shown in Fig. 21, where $i_L^*=20$ A and $v_{\rm dc1}=100$ V. As can be shown in Fig. 21, $v_{\rm M1}$ is a rectangular wave that has an ac component and an average dc component. The frequency of the ac component is 900 Hz. It can be observed that the duty ratio of S_1, $d_{\rm M}$, is slightly larger than half $(=v_{\rm dc2}/(v_{\rm dc1}+v_{\rm dc2}))$ because the average-voltage control adds a voltage component to the feedforward component given by (6). $v_{\rm M2}$ is similar to $v_{\rm M1}$ in its shape, and it has a duty ratio of $1-d_{\rm M}$. The auxiliary converter eliminates the 900-Hz ac component contained within $v_{\rm M1}-v_{\rm M2}$, and only the ripple voltage resulting from the PSPWM contributes to the ripple current generation.

The dc-capacitor voltages, v_{C1}, v_{C2}, and v_{C3}, have a 50-V dc component, and a 900-Hz ac component that has a peak-to-peak value that is acceptable, as mentioned above.

The current sourced from $v_{\rm dc1}$, $i_{\rm dc1}$, is a rectangular wave with a principal frequency of 900 Hz. Furthermore, the dc current flowing to $v_{\rm dc2}$, $i_{\rm dc2}$, is similar in shape to $i_{\rm dc1}$. It should be noted that these 900-Hz components can be attenuated by applying *LC* filters designed appropriately at the $v_{\rm dc1}$ and $v_{\rm dc2}$ sides, which is a well-established method that is also applicable to the conventional NIBB. The active power flow between $v_{\rm dc1}$ and $v_{\rm dc2}$ is indirectly controlled by controlling i_L. Fig. 21 shows that i_L is regulated at 20 A.

D. Steady-State Behavior in Boost Mode

The steady-state behavior of the NIBAC during boost operation is shown in Fig. 22, where $i_L^*=20$ A and $v_{\rm dc1}=50$ V. As can be seen in Fig. 22, $v_{\rm M1}$ is equal to $v_{\rm dc1}$ because S_1 is kept ON and S_2 is kept OFF during this mode of operation. Meanwhile, $v_{\rm M2}$ is a rectangular wave that has an ac component and an average dc component. It can be observed that the duty ratio of S_4, $d_{\rm M}$, is slightly less than half $(=(v_{\rm dc2}-v_{\rm dc1})/v_{\rm dc2})$ because the average-voltage control adds a negative voltage component to the feedforward component given by (6). The auxiliary converter eliminates the 900-Hz ac component contained within $v_{\rm M1}-v_{\rm M2}$, and only the ripple voltage resulting from the PSPWM contributes to the ripple-current generation.

The dc-capacitor voltages, v_{C1}, v_{C2}, and v_{C3}, have a 50-V dc component and a 900-Hz ac component that has a peak-to-peak value that is acceptable, as mentioned above.

The current sourced from $v_{\rm dc1}$, $i_{\rm dc1}$, is a rectangular wave with a principal frequency of 900 Hz. Furthermore, the dc current flowing to $v_{\rm dc2}$, $i_{\rm dc2}$, is similar in shape to $i_{\rm dc1}$. The active power

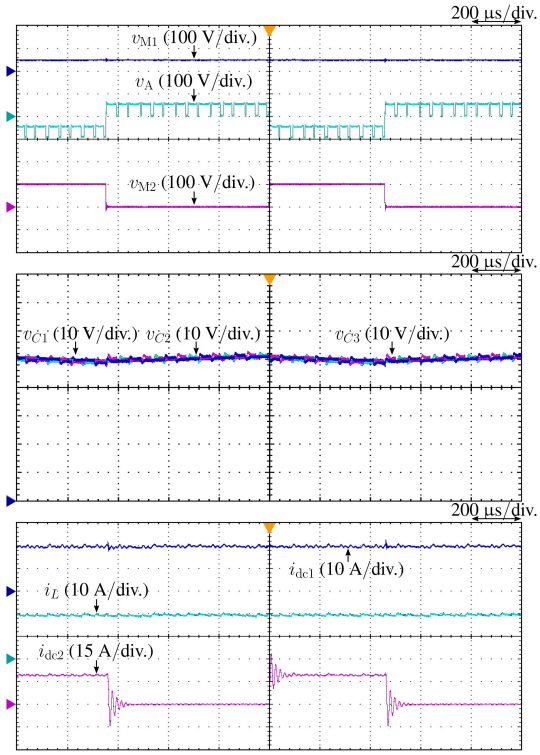

Fig. 22. Experimental waveforms of the NIBAC operating in boost mode.

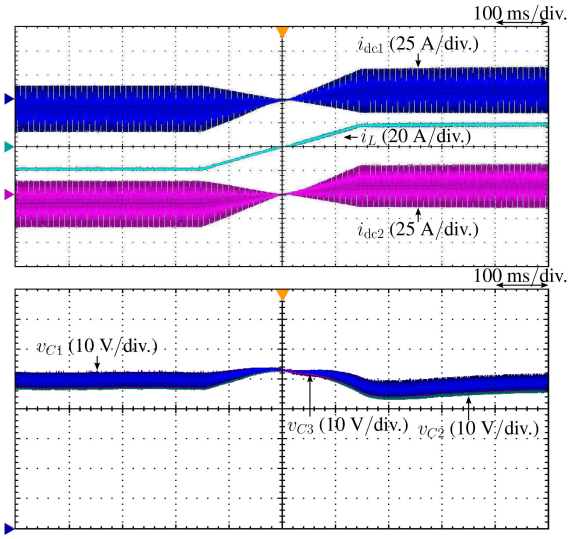

Fig. 23. Experimental waveforms of the NIBAC operating in buck–boost mode during a ramp change in i_L^* from -20 to 20 A in 300 ms.

flow between v_{dc1} and v_{dc2} is indirectly controlled by controlling i_L. Fig. 22 shows that i_L is regulated at 20 A.

E. Transient Behavior During a Ramp Change in i_L in Buck–Boost Mode

The transient-state behavior of the NIBAC when $v_{dc1} = 100$ V and i_L^* ramps up from -20 to 20 A in 300 ms is depicted in Fig. 23, which shows that i_L follows its reference value without overcurrent. Similarly, i_{dc1} and i_{dc2} obey the ramp behavior.

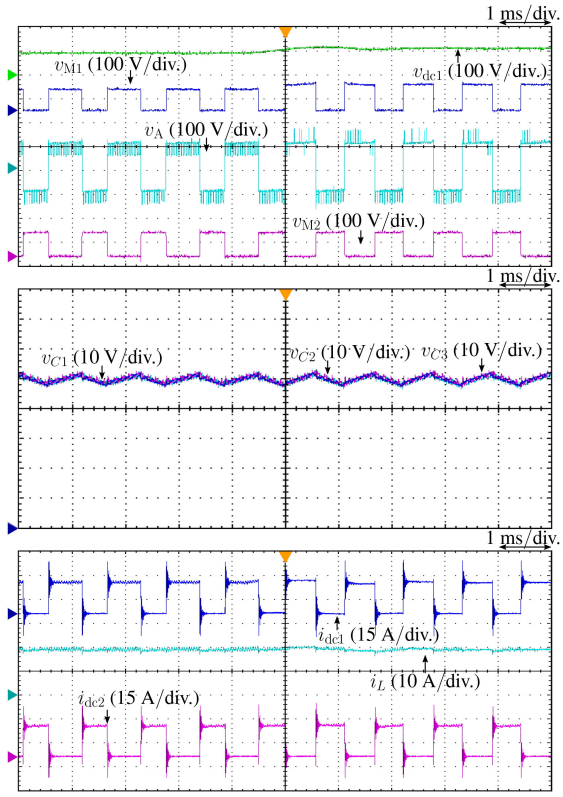

Fig. 24. Experimental waveforms of the NIBAC operating in buck–boost mode during a step change in v_{dc1} from 90 to 110 V.

Examination of Fig. 23 shows that the slope of i_L decreases when it approaches zero. This decrease in the slope results from the ON-state voltages of switching devices employed in the auxiliary converters. This effect can be attenuated by applying the ON-state voltage drop compensation method. After the end of the transient period, the dc components contained within each dc-capacitor voltage regain the values they had prior to the ramp occurrence.

F. Transient Behavior During a Step Change in v_{dc1} in Buck–Boost Mode

The transient-state behavior of the NIBAC when $v_{dc2} = 100$ V, $i_L = 20$ A, and a step change from 90 to 110 V occurs in v_{dc1} is shown in Fig. 24. v_{dc1} shown in Fig. 24 deviates from the step-change manner because of the dc-link capacitance. It can be shown that v_{M1} changes according to the change in v_{dc1}, and the control system has a very fast response as can be observed from the change in v_A. The change in the remaining waveforms is almost unnoticeable indicating a robust control system.

VII. Conclusion

This article has proposed a noninverting bidirectional chopper with an auxiliary converter (NIBAC) that is characterized by operating in buck, buck–boost, and boost modes and has a significantly lower mass and volume compared with the four-switch NIBB and the TL-NIBB, where according to the comparison made in this study, a reduction in the inductance value by a

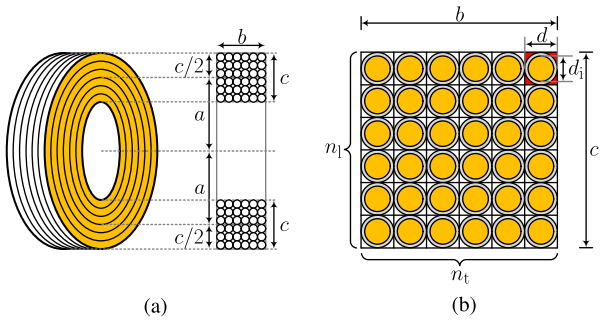

Fig. 25. Cylindrical multilayer air-core inductor with rectangular cross section. (a) Inductor dimensions. (b) Winding dimensions.

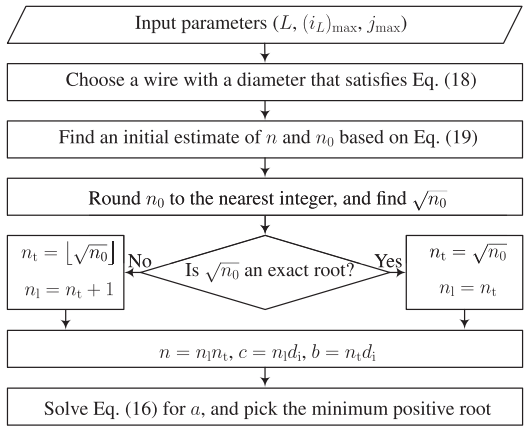

Fig. 26. Flowchart of multilayer air-core inductor design.

factor of 59 and 30 can be achieved when the NIBAC is used instead of the NIBB and the TL-NIBB, respectively. The loss analysis of the chopper has shown that high chopper efficiency can be achieved even though an auxiliary converter is applied. These conclusions suggest that the proposed chopper shows promise as a chopper for onboard BESSs. The efficacy of the NIBAC along with the associated control system has been confirmed by conducting experiments using a down-scaled prototype.

APPENDIX

To estimate the volume of the inductors used in the candidate choppers, multilayer air-core inductors were designed. Fig. 25 shows an air-core inductor with a rectangular cross-section, where a is the distance between the axis of the winding and the axis of the inductor, b is the width of the winding cross section, c is the height of the winding cross-section, n_l is the number of layers, n_t is the number of turns per layer, d is the wire diameter excluding the insulation coating, and d_i is the wire diameter including the insulation coating. The inductance value of the inductor shown in Fig. 25 can be given by

$$L = \frac{\mu_0 n^2 \pi a^3}{ab + 0.9a^2 + 0.32bc + 0.84ac} \tag{16}$$

where μ_0 is the vacuum permeability, and n is the number of turns. To obtain maximum inductance for a given length of wire, Brooks coil geometry is used, where $b = c$, and $a = 1.5c$. The inductance value of the Brooks coil can be given by

$$L = 2.029\mu_0 c n^2. \tag{17}$$

To prevent the inductor from overheating, a current density limit, $j_{\max}$, should not be exceeded. d can be determined from $j_{\max}$ and the maximum rms value of the inductor current, $(i_L)_{\max}$, as

$$d = \sqrt{\frac{4(i_L)_{\max}}{\pi j_{\max}}}. \tag{18}$$

For the inductors designed in this article, $j_{\max}$ is set to $2 \times 10^6 \mathrm{A/m^2}$ as a practical value to avoid inductor overheating [26]. After that, an initial estimate of the number of turns, n_0, for a given inductance value can be calculated if Brooks geometry is assumed, where n_0 can be given by

$$n_0 = \sqrt[5]{\left(\frac{L}{2.029\mu_0 d_i}\right)^2}. \tag{19}$$

If $\sqrt{n_0}$ is not an exact root, this means that the condition $b = c$ cannot be satisfied. Therefore, n_t is selected as the floor of $\sqrt{n_0}$, $\lfloor \sqrt{n_0} \rfloor$, and additional layer is added. After that, b, c, and n can be recalculated, and a can be found by solving (16) for a. A flowchart of the multilayer air-core inductor design is shown in Fig. 26.

The volume of the inductor, v_{ir}, is basically a volume of a cylinder, and it can be given by

$$v_{ir} = \pi b \left(a + \frac{c}{2}\right)^2. \tag{20}$$

To estimate the mass of the inductor m_{ir} it is assumed that m_{ir} is the mass of the conductor and it can be given by

$$m_{ir} = \rho v_{cr} \tag{21}$$

where ρ is the mass density of the conductor material, and v_{cr} is the volume of the conductor. From the volume of the coil and a winding packing factor, k_p, v_{cr} can be approximated and it can be given by

$$v_{cr} = k_p v_{cl} c \tag{22}$$

where k_p is the fraction of the volume occupied by the conductors to the total volume of the coil, and it can be estimated from the winding area packing factor (i.e., cross-sectional area of the conductor/cross-sectional area of the the coil $= (\pi/4)(d/d_i)^2$). The coil volume v_{cl} is a volume of a hollow cylinder and it can be given by

$$v_{cl} = 2\pi abc. \tag{23}$$

To estimate the inductor losses, the dc resistance of the inductor R_{dc} should be calculated. R_{dc} can be given by

$$R_{dc} = \frac{2\pi n^2 a}{k_p \sigma bc} \tag{24}$$

where σ is the electrical conductivity of the conductor material.

REFERENCES

[1] A. Khaligh and Z. Li, "Battery, ultracapacitor, fuel cell, and hybrid energy storage systems for electric, hybrid electric, fuel cell, and plug-in hybrid electric vehicles: State of the art," *IEEE Trans. Veh. Technol.*, vol. 59, no. 6, pp. 2806–2814, Jul. 2010.

[2] C. Wu, S. Lu, F. Xue, L. Jiang, and M. Chen, "Optimal sizing of onboard energy storage devices for electrified railway systems," *IEEE Trans. Transport. Electrific.*, vol. 6, no. 3, pp. 1301–1311, Sep. 2020.

[3] D. Yildirim *et al.*, "Full-scale physical simulator of all SiC traction motor drive with onboard supercapacitor ESS for light-rail public transportation," *IEEE Trans. Ind. Electron.*, vol. 67, no. 8, pp. 6290–6301, Aug. 2020.

[4] S. Faddel, A. A. Saad, T. Youssef, and O. Mohammed, "Decentralized control algorithm for the hybrid energy storage of shipboard power system," *IEEE Trans. Emerg. Sel. Topics Power Electron.*, vol. 8, no. 1, pp. 720–731, Mar. 2020.

[5] B. Zahedi and L. E. Norum, "Modeling and simulation of all-electric ships with low-voltage DC hybrid power systems," *IEEE Trans. Power Electron.*, vol. 28, no. 10, pp. 4525–4537, Oct. 2013.

[6] K. Bellache, M. B. Camara, and B. Dakyo, "Transient power control for diesel-generator assistance in electric boat applications using supercapacitors and batteries," *IEEE Trans. Emerg. Sel. Topics Power Electron.*, vol. 6, no. 1, pp. 416–428, Mar. 2018.

[7] H. Zhang, F. Mollet, C. Saudemont, and B. Robyns, "Experimental validation of energy storage system management strategies for a local DC distribution system of more electric aircraft," *IEEE Trans. Ind. Electron.*, vol. 57, no. 12, pp. 3905–3916, Dec. 2010.

[8] A. Gómez-Expósito, J. M. Mauricio, and J. M. Maza-Ortega, "VSC-based MVDC railway electrification system," *IEEE Trans. Power Del.*, vol. 29, no. 1, pp. 422–431, Feb. 2014.

[9] A. Verdicchio, P. Ladoux, H. Caron, and S. Sanchez, "Future DC railway electrification system - Go for 9 kV," *IEEE Int. Conf. Elect. Syst. Aircr., Railway, Ship Propul. Road Veh. Int. Transp. Electrific. Conf.*, 2018, pp. 1–5.

[10] V. I. Herrera, H. Gaztañaga, A. Milo, A. Saez-de-Ibarra, I. Etxeberria-Otadui, and T. Nieva, "Optimal energy management and sizing of a battery-supercapacitor-based light rail vehicle with a multiobjective approach," *IEEE Trans. Ind. Appl.*, vol. 52, no. 4, pp. 3367–3377, Jul./Aug. 2016.

[11] A. Allègre, A. Bouscayrol, J. Verhille, P. Delarue, E. Chattot, and S. El-Fassi, "Reduced-scale-power hardware-in-the-loop simulation of an innovative subway," *IEEE Trans. Ind. Electron.*, vol. 57, no. 4, pp. 1175–1185, Apr. 2010.

[12] F. Ciccarelli, A. Del Pizzo, and D. Iannuzzi, "Improvement of energy efficiency in light railway vehicles based on power management control of wayside lithium-ion capacitor storage," *IEEE Trans. Power Electron.*, vol. 29, no. 1, pp. 275–286, Jan. 2014.

[13] M. Pavlovský, G. Guidi, and A. Kawamura, "Assessment of coupled and independent phase designs of interleaved multiphase buck/boost DC-DC converter for EV power train," *IEEE Trans. Power Electron.*, vol. 29, no. 6, pp. 2693–2704, Jun. 2014.

[14] O. Hegazy, J. V. Mierlo, and P. Lataire, "Analysis, modeling, and implementation of a multidevice interleaved DC/DC converter for fuel cell hybrid electric vehicles," *IEEE Trans. Power Electron.*, vol. 27, no. 11, pp. 4445–4445, Nov. 2012.

[15] K. Takao *et al.*, "High-power converters with high switching frequency operation using SiC-PiN diodes and Si-IEGTs," in *Proc. 1st Int. Conf. Electr. Power Equip. - Switching Technol.*, 2011, pp. 412–417.

[16] N. Soltau *et al.*, "Electric-energy savings using 3.3 kV full-SiC power modules in traction applications," in *Proc. 15th Int. Conf. Ecol. Veh. Renewable Energies*, 2020, pp. 1–5.

[17] K. Yasui *et al.*, "A 3.3 kV 1000 a. high power density SiC power module with sintered copper die attach technology," in *Proc. PCIM Eur., Int. Exhib. Conf. Power Electron., Intell. Motion, Renewable Energy Manage.*, Nuremberg, Germany, 2019, pp. 312–317.

[18] F. Caricchi, F. Crescimbini, and A. Di Napoli, "20 kW water-cooled prototype of a buck-boost bidirectional DC-DC converter topology for electrical vehicle motor drives," in *Proc. IEEE Appl. Power Electron. Conf. Expo.*, Dallas, TX, USA, 1995, pp. 887–892.

[19] M. A. Khan, A. Ahmed, I. Husain, Y. Sozer, and M. Badawy, "Performance analysis of bidirectional DC-DC converters for electric vehicles," *IEEE Trans. Ind. Appl.*, vol. 51, no. 4, pp. 3442–3452, Jul./Aug. 2015.

[20] H. Lee and J. Yun, "High-efficiency bidirectional buck-boost converter for photovoltaic and energy storage systems in a smart grid," *IEEE Trans. Power Electron.*, vol. 34, no. 5, pp. 4316–4328, May 2019.

[21] K. Ogura, K. Nishimura, and Y. Oku, "A bidirectional DC-DC converter for battery electric light rail vehicle and its test run results," in *Proc. Int. Conf. Power Electron. Drive Syst.*, 2019, pp. 1–6.

[22] H. J. Ahmad and M. Hagiwara, "Interleaved bidirectional chopper with auxiliary converters for DC electric railways," *IEEE Trans. Power Electron.*, vol. 36, no. 5, pp. 5336–5347, May 2021.

[23] Y. l. Cao, Y. Jiang, Z. Tang, and W. Tan, "Research on different carrier phase-shifted angle with output voltage performance of cascade multilevel inverter," in *Proc. IEEE 6th Int. Power Electron. Motion Control Conf.*, 2009, pp. 1448–1451.

[24] F. Li, R. Hao, H. Lei, X. You, C. Ke, and J. Wang, "Non-inverting three-level buck-boost converter for wide voltage range application," in *Proc. IEEE Energy Convers. Congr. Expo.*, Portland, OR, USA, 2018, pp. 4870–4875.

[25] G. Abad, *Power Electronics and Electric Drives for Traction Applications*. Hoboken, NJ, USA: Wiley, 2016.

[26] R. Barrera-Cardenas, T. Isobe, and M. Molinas, "Optimal design of air-core inductor for medium/high power DC-DC converters," in *Proc. IEEE 17th Workshop Control Model. Power Electron.*, 2016, pp. 1–8.

[27] A. Hillers, M. Stojadinovic, and J. Biela, "Systematic comparison of modular multilevel converter topologies for battery energy storage systems based on split batteries," in *Proc. IEEE Eur. Conf. Power Electron. Appl.*, Geneva, Switzerland, 2015, pp. 1–9.

[28] J. Choi, B. Han, and H. Kim, "New scheme of phase-shifted carrier PWM for modular multilevel converter with redundancy submodules," *IEEE Trans. Power Del.*, vol. 31, no. 1, pp. 407–409, Feb. 2016.

[29] 2020. [Online]. Available: https://www.hitachi-power-semiconductor-device.co.jp/en/products/igbt/pdf/IGBT-SP-12023R6MBM250H33E3web.pdf

[30] 2020. [Online]. Available: https://americas.fujielectric.com/wp-content/uploads/2020/06/2MBI200XAA120-50.pdf

[31] 2020. [Online]. Available: https://www.electronicon.com/fileadmin/inhalte/pdfs/downloadbereich/Katalog/neueKataloge/200.003-020030PK16.pdf

Hamzeh J. Ahmad (Student Member, IEEE) was born in Amman, Jordan, in 1991. He received the B.S. degree in electrical engineering from Hashemite University, Zarqa, Jordan, in 2013, and the M.S. degree in electrical engineering\power and control from the Jordan University of Science and Technology, Irbid, Jordan, in 2016. He is currently working toward the Ph.D. degree in electrical and electronic engineering with the Tokyo Institute of Technology, Meguro City, Japan.

His research interests include high-power dc-to-dc converters for electric trains/vehicles, dc-to-ac converters for utility applications, solid-state circuit breakers, and control of power converters.

Makoto Hagiwara (Senior Member, IEEE) was born in Tokyo, Japan, in 1979. He received the B.S., M.S., and Ph.D. degrees in electrical engineering from the Tokyo Institute of Technology, Meguro City, Japan, in 2001, 2003, and 2006, respectively.

From April 2006 to March 2015, he was an Assistant Professor with the Department of Electrical and Electronic Engineering, Tokyo Institute of Technology, and has been an Associate Professor, since April 2015. The total citation index for all his papers in Google Scholar is more than 5700. His research interests include dc-to-dc converters for electric trains/vehicles, high-voltage high-power converters for utility applications and renewable energies, and HVdc technologies.

Dr. Hagiwara was the recipient of the 2010 international power electronics conference (IPEC-Sapporo/ECCE-Asia) Second Prize Paper award, the 2012 and 2013 IEEE Industry Applications Society Industrial Power Converter Committee First Prize Paper Awards, and the 2014 Isao Takahashi Power Electronics Award.